Journal of Membrane Science 713 (2025) 123374

Contents lists available at ScienceDirect

Journal of Membrane Science

journal homepage: www.elsevier.com/locate/memsci

Built-in elasticity-rigidity balanced polymer electrolyte in solid-state Li-batteries with high-loading cathode

Weichen Han [a,1], Jingang Zheng [a,1], Hao Huang [a], Hongxu Zhou [a], Hongyang Li [a], Han Zhang [a], Lixiang Li [a,**], Weimin Zhou [a], Baigang An [a], Chengguo Sun [a,b,*]

[a] School of Chemical Engineering, University of Science and Technology Liaoning, Anshan, 114051, PR China
[b] School of Chemical Engineering, Nanjing University of Science and Technology, Nanjing, Jiangsu, 210094, PR China

ARTICLE INFO

Keywords:
Elasticity-rigidity balance
Crosslinking polymerization
High-loading electrodes
Solid-state lithium batteries

ABSTRACT

Solid-state lithium batteries (SSLBs) using polymer electrolytes have attracted increasing attention owing to their intrinsic flexibility and high energy density. However, due to the lack of permeability like liquid electrolytes, polymer electrolytes equipped with high-loading electrodes are usually limited by the high polarization and rapid capacity decay. Herein, an elasticity-rigidity balanced polymer electrolyte (ERBE) was designed by the in-situ crosslinking polymerization, where poly(ethylene glycol) diacrylate (PEGDA) works as crosslinking elasticity agents, poly(vinylidene carbonate) (PVC) acts as main structure support. Benefiting from the structural design, ERBE electrolyte features high compression strength of 96.1 MPa and volume compression ratio up to 73.9 %. The ERBE also exhibits room-temperature ionic conductivity of 2.31×10^{-4} S cm^{-1} and high Li-ions transfer number of 0.69. The $LiFePO_4$||Li cells equipped with ERBE electrolyte can maintain over 3000 cycles with 70.1 % capacity retention at 1 C and 25 °C. Even at the cathode mass loading up to 78 mg cm^{-2}, it can deliver a high discharge capacity of 11.98 mAh cm^{-2} at 25 °C. Such an integrated in-situ polymer electrolyte provides strong support for solving the problems of rigidity or elasticity insufficiency and dendrite growth, and holds promising applications in wide-temperature, high-energy-density solid-state batteries.

1. Introduction

Solid-state lithium batteries (SSLBs) are regarded as the most promising next-generation energy storage technology, owing to their high security, high energy density, and long lifespan [1–3]. Among the most significant structural components of SSLBs, solid-state electrolytes (SSEs) work as functional bridge for Li-ions transport that directly determines the performance of the SSLBs [4]. However, the SSEs lack fluidity and wettability like liquid electrolyte, it is difficult for SSLBs to overcome the high interfacial resistances and slow Li-ions transport kinetics, especially for Li-ions/electron transport within the high mass loading cathode electrodes. Therefore, designing SSEs with good compatibility and wettability that suitable for high-loading electrodes is one of the main challenges for SSLBs.

To address the suitability of SSLBs with high-loading electrodes, the introduction of conductive additives or protective layers at electrode and electrolyte interfaces has been used to enhance the efficiency of Li-ions/electron transport and increase the interface contact [5–7]. For example, in-situ polymerization reaction strategy [8], laser-induced technology [9] and atomic layer deposition technique [10] have achieved significant results in reducing interfacial resistance and improving the cyclic stability of SSLBs. However, due to the absence of additional medium in high-loading electrodes for accelerating Li-ions transport, most of the mass loading of cathodes based on SSLBs are still limited at a low level, hardly exceeding 10 mg cm^{-2} [11]. To enhance the interfacial contact between electrolyte and thick electrode, and construct efficient Li-ions transport networks within the electrode [12–15], adding the oxides conductors [16–18], metal halides [19] or solid-state electrolyte components [20] in thick electrodes have been reported and significant progress have been made in reducing polarization and improving cycling stability of the high-loading SSLBs. More importantly, beside the above-mentioned strategies for the modification of electrode and

* Corresponding author. School of Chemical Engineering, University of Science and Technology Liaoning, Anshan, 114051, PR China.
** Corresponding author.
E-mail addresses: lxli2005@126.com (L. Li), sunyangguo2004@163.com (C. Sun).
[1] They contributed equally to this work.

https://doi.org/10.1016/j.memsci.2024.123374
Received 29 July 2024; Received in revised form 16 September 2024; Accepted 27 September 2024
Available online 27 September 2024

electrolyte, further considerations need to be given, including approaches to ensure the continuous distribution of Li-ions conductors within thick cathode, and the improvement of processing techniques. Compared to the introduction of additional auxiliary additives, The in-situ polymer electrolyte not only serves as a 'bridge' to transport Li-ions between cathode and Li-anode, but also allows for constructing an abundant Li-ions transport networks in thick electrodes due to the high permeability of the liquid precursor. Consequently, an elasticity-rigidity balanced polymer electrolyte in the perspective of structural composition was designed, which features excellent wettability and maintains low polarization voltage with thick electrode. The rigid PVC containing appropriate lithium salts has been proven to possess a high room temperature Li-ions conductivity up to 10^{-4} S cm^{-1} [21], which is preferred for the construction of fast Li-ions conductor and inhibition of dendrite growth. To balance the intrinsic rigidity and elasticity of the PVC-based electrolyte, the elastic polymerized PEGDA was selected as the crosslinker because it can easily crosslink with the vinylidene carbonate (VC) monomer and form a desirable crosslinked polymer structure.

Herein, a facile polymer electrolyte with highly elasticity-rigidity balance property was constructed by the in-situ crosslinking polymerization. The improvement of elasticity function is assigned from PEGDA, and polymerized VC acts as rigid structural support. To achieve the stable interface layers, a small doses of 1,3-propane sultone (PS) as an interface layer-forming agent was added. As shown in Fig. 1, the flowable ERBE precursor was injected into the cells to adequately penetrate cathode and lithium metal anode, allowing for the construction of Li-ions channels and ensuring good electrode/electrolyte contact. The Li||Li cells cycled over 2000 h at 0.5 mA cm^{-2} without obvious dendrite growth. The $LiFePO_4$(LFP)||Li cells (4 mg cm^{-2}) equipped with ERBE have excellent initial discharge capacity of 140.7 mAh g^{-1} at 25 °C and 1 C, as well as superior cycling stability of 1400 cycles (80 % capacity retention), 3000 cycles (70.1 % capacity retention), and even cycled over 4000 cycles, which still can deliver a discharge capacity of 75.6 mAh g^{-1}. Even at −10 °C, the cells still demonstrate a stable cycling performance with a high capacity retention of 95 % over 200 cycles at 0.1 C. More importantly, benefiting from the excellent infiltration ability and Li-ions transport properties, the ERBE can match high-loading LFP cathodes up to 78 mg cm^{-2} and provide a high capacity of 11.98 mAh cm^{-2} at 25 °C.

2. Experimental

2.1. Materials

VC (99.9 %), LiTFSI (99.8 %), PS (99 %), cellulose diaphragm (TF4030) were purchased from DoDoChem Co., Ltd. PEGDA (M_w:~400) from Energy Chemical Co., Ltd. Super P, polyvinylidene fluoride (PVDF) were purchased from Shenzhen Kejingstar Technology Co., Ltd. 2,2′-Azobis(2-methylpropionitrile) (AIBN, 98 %), N-Methyl pyrrolidone (NMP) were purchased from Macklin Co., Ltd. Lithium metal was purchased from Tianjin Zhongneng Lithium Industry Co., Ltd.

2.2. Preparation of ERBE-based solid-state electrolytes

Synthesis of Materials: A solution was obtained by dissolving 0.6 g of LiTFSI in 1 g of VC, 0.15 g of PEGDA, 60 mg of PS, and 6 mg of AIBN. Then followed by stirring until clear and transparent at 60 °C. The solution was injected into 2032 coin cell, where cellulose separator was adopted to separate the cathode from the anode. Later, the cells were kept constantly at 60 °C for 12 h in vacuum oven to generate the completion of polymerization of ERBE.

$LiFePO_4$ or $LiNi_{0.3}Mn_{0.3}Co_{0.3}O_2$(NCM333), Super P, PVDF were mixed in NMP with stirring (mass ratio, LFP or NCM333: SP: PVDF = 8: 1: 1), the prepared slurry was cast on aluminum current collector and dried at 80 °C under vacuum overnight before used. The mass loading of LFP or NCM333 was above 4 mg cm^{-2}. For high mass loading cathodes, the LFP:SP:PVDF ratio is adjusted to 9:0.5:0.5, and the mass loading was between 4 and 78 mg cm^{-2}, the density of the thick electrodes is in the range of 2.75–3.05 g cm^{-3}.

2.3. Physical characterization

The X-ray diffraction (XRD) and Fourier Transform Infrared Spectrometer (FTIR) were measured by D8 with Cu Ka radiation, and ALPHA II, Bruker Corporation.

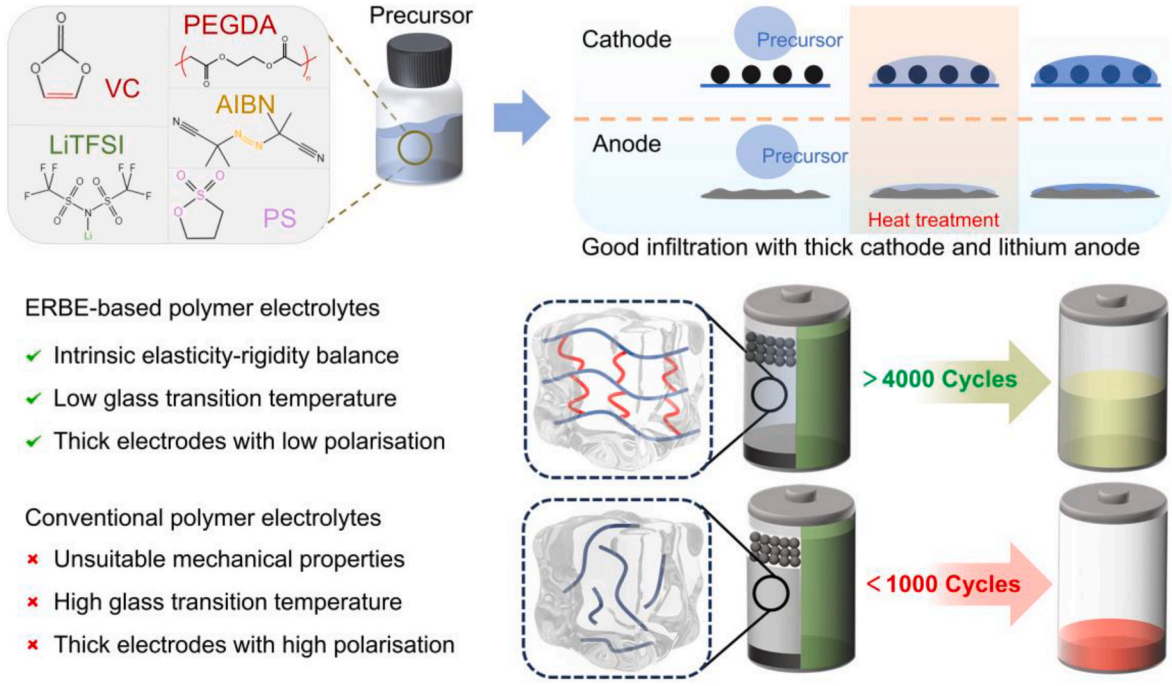

Fig. 1. Schematic of ERBE electrolyte infiltration and the performance benefits.

The ionic conductivity σ was calculated from the following equation:

$$\sigma = \frac{d}{S \times R_b}$$

where d (cm) is the thickness of the polymer electrolyte membrane, S (cm^2) is the area of the stainless-steel electrode, and R_b (Ω) is the bulk resistance of the electrolyte membrane measured by EIS.

The activation energy (E_a) was calculated from Arrhenius formula (Equation (3))

$$\sigma = A\exp\left(\frac{E_a}{RT}\right)$$

The Li^+ transfer number (t_{Li+}) of solid polymer electrolyte was measured using chronoamperometry test on the Li||electrolyte||Li cells with applied voltage of 0.01 V, t_{Li+} was calculated by following equation:

$$t_{Li+} = \frac{I_s(\Delta V - I_0 R_0)}{I_0(\Delta V - I_s R_s)}$$

where ΔV (V) is the potential applied across the cell, the initial (I_0) and steady-state (I_s) currents are obtained from the chronoamperometric curve. R_0 and R_s measured by EIS, reflect the initial and steady-state resistances of the passivating layers.

The elastic modulus of the solid polymer electrolyte was measured by preparing a standard square sample with a side length of 10 mm for the uniform compression test, and the elastic modulus was measured by the stress-strain experiment. The elastic modulus was calculated by the following formula:

$$E = \frac{F\,L}{S\,dL}$$

where F is the stress applied to the specimen, S is the stressed area of the specimen, and L is the length of ERBE electrolyte. The degree of deformation (dL) is derived from the test data.

As for the Shore hardness test, ERBE electrolytes were prepared as cylinders with 15 mm diameter and 23 mm height to test the Shore hardness. Five points were selected for testing to ensure the accuracy of the data.

2.4. Characterization instrument

The microstructure and morphologies of the samples were analyzed by scanning electronic microscopy (SEM, Thermo Fisher Scientific Apreos). Energy dispersive spectrometer (EDS) was performed to determine the composition of cathode. The X-ray photoelectron spectroscopy (XPS) was measured by AXIS-SUPRA, KRATOS. Thermogravimetric analysis (TGA) was conducted on TA Instruments-Waters LLC up to 700 °C under N_2 atmosphere with 10 °C min^{-1}. Differential scanning calorimetry (DSC) tests were performed on DSC2-01271 thermal analyzer from −80 to 100 °C under N_2 atmosphere with 5 °C min^{-1}. The Compressive stress test on INSTRON 5982 electronic universal testing machine. The microstructure and composition of SEI and CEI layers were analyzed by a transmission electron microscope (JEM-F200 (URP)).

3. Results and discussion

3.1. Preparation and characterization of ERBE membrane

The ERBE was prepared by crosslinking polymerization of VC and PEGDA with moderate doses of LiTFSI. AIBN as the radical initiator was employed to promote the conversion of liquid ERBE precursor to solid-state polymer at 60 °C for 12 h (Fig. 2a). As seen in Fig. 2b, the FTIR further proved the crosslinking polymerized between VC and PEGDA, due to the peak at 3164 and 1600 cm^{-1} corresponding to = C–H and –C═C bonds of alkenes disappeared after heat treatment. In addition, the peak at 1636 cm^{-1} of C═O bond was enhanced, indicating the Li-

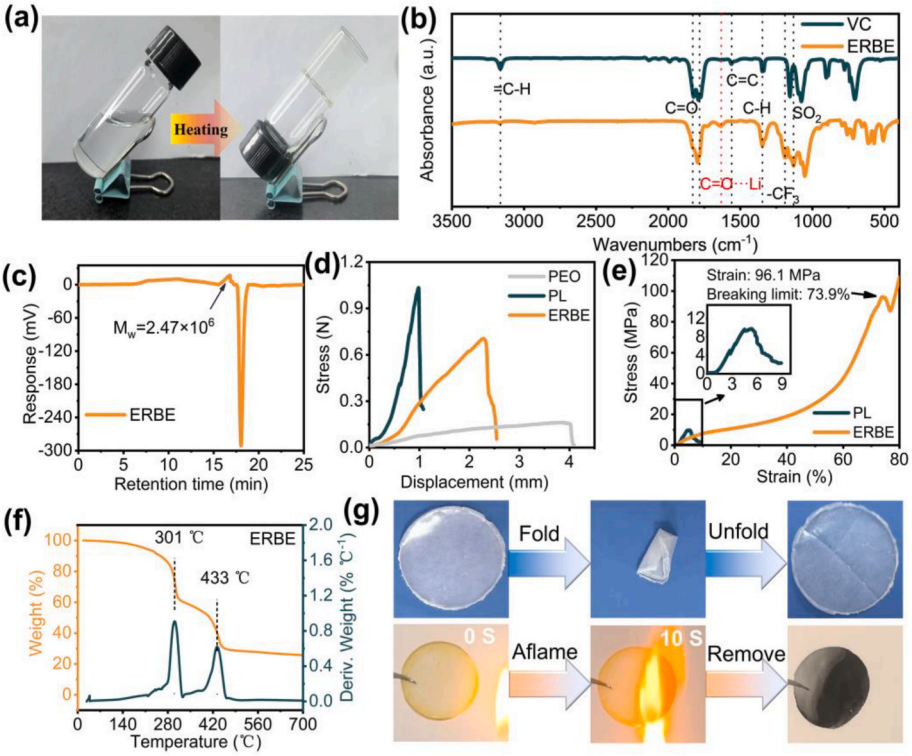

Fig. 2. (a) Optical images of ERBE before and after heat curing. (b) Fourier-transform infrared spectroscopy (FTIR) spectra of the VC and ERBE. (c) Gel permeation chromatography (GPC) curve of ERBE. (d) Puncture experiments for PEO, PL and ERBE with 0.5 mm diameter steel needle. (e) Stress-strain curves of the PL and ERBE. (f) Thermogravimetric curve of ERBE. (g) Flexible and retardant properties of ERBE.

ions dissociated from LiTFSI participated in the coordination with the ERBE structure [22]. To further investigate the degree of crosslinking polymerization between PVC and PEGDA, the contrast sample electrolyte without PEGDA was also prepared and abbreviated as PL. Their molecular weights were measured by GPC method. It can be found that the weight-average molecular weight increased from 1.72×10^6 g mol^{-1} for PL to 2.47×10^6 g mol^{-1} for ERBE (Fig. 2c and S1), indicating that the VC and PEGDA can be well cross-linked copolymerized to form integrated networks structure.

The compression and puncture tests were carried out to further demonstrate the elasticity-rigidity balance of ERBE. Both polyethylene oxide (PEO) and PL electrolyte film were referenced as comparison sample for more visualization. As shown in Fig. 2d, the forces for puncturing PL, ERBE and PEO were 0.98, 0.72 and 0.16 N, respectively. Compression test results show that the corresponding anti-breaking strain of ERBE can reach 96.1 MPa, which is 32 times higher than that of PL (Fig. 2e). These results demonstrate that the introduction of PEGDA into PL can lower the rigidity of polymerized VC, while increase the flexibility, leading to that ERBE has good elasticity rigidity balance. To further visually evaluate the effect of PEGDA on the rigidity and elasticity balance, PVC-based electrolytes with 5 %, 15 %, 25 %, and 35 % PEGDA were prepared. As shown in Fig. S2, samples of PVC-based electrolytes with contents of 5 %, 25 % and 35 % were fractured at certain pressures, and only the working sample (15 %) remained structurally whole for more than 50 % of bending. The above results show that the PVC-based electrolyte with 15 % PEGDA exhibits an excellent balance of rigidity and elasticity. As showing in Fig. S3, further testing the pensile properties and Shore hardness of the ERBE electrolyte, showing that the ERBE electrolyte has an excellent Young's modulus (31.0 MPa) and Shore hardness (57.2 HD). The thermal stability of ERBE was determined by thermogravimetric analysis (TGA). As shown in Fig. 2f and S4, with the temperature increased, two weight loss steps are distinguished in the thermogravimetric curve, the first stage between 136 and 345 °C is attributable to oligomeric molecules and trace monomer solutions, the second weight loss begins from around 350 to 470 °C is caused by degradation of the LiTFSI [23]. In contrast to the decomposition temperature of PL from the starting value of 66 °C, indicating that the networks structure of crosslinked ERBE possesses a more stable thermal stability at the molecular level. The safety and flexibility are further confirmed by the harsh abuse and combustion tests and shown in Fig. 2g. The ERBE remains the original configuration after arbitrary bending and folding, showing good flexibility (Fig. 2g).

3.2. Electrochemical properties of ERBE

As seen in Fig. S5, The XRD peak intensity at around 20° of PVC was significantly reduced by the introduction of PEGDA and LiTFSI, suggesting that the structure of ERBE tends to be amorphous, facilitating rapid and uniform migration of Li-ions within the electrolyte. DSC measurement was conducted to further determine the thermal transition of ERBE electrolyte. Fig. 3a shows that the glass transition temperature (T_g) of ERBE electrolyte reaches −55.8 °C, which is much lower than the 47.5 °C of PL (Fig. S6). Generally, low T_g ensures the stability of Li-ions transport in a wide temperature range [20]. Raman spectra was employed to further investigate the Li-ions conduction in ERBE electrolyte. Fig. 3b and S7 show the stretching vibrations of N–S bonds from $TFSI^-$ in ERBE and PL electrolytes. In the ERBE electrolyte, after fine fitting the spectra, the ratio of free-state $TFSI^-$ to undissociated $TFSI^-$ is 96.35 %, which is higher than that in PL (79.55 %). This is attributed to the significant increase in the amorphous region of the ERBE electrolyte, which provides more free volume space for the dissociation and conduction of lithium salts. In addition, PEGDA in PVC-based polymers is not only a crosslinking agent, but also a functional ionic conductor to promote the dissociation of lithium salts. Therefore, the above synergistic effect will significantly enhance the dissociation of lithium salts by the ERBE electrolyte. suggesting that the Li-ions is more easily dissociate from LiTFSI in ERBE, thus allowing more free Li-ions to migrate during charge and discharge [23]. To further investigate the Li-ions transport properties in ERBE, electrochemical impedance spectroscopy (EIS) was used to investigate the Li-ions conductivity. As shown in Fig. 3c–S8, and S9, after fitting with Arrhenius law, the Li-ions conductivity of ERBE (2.31×10^{-4} S cm^{-1}) was slightly higher than that of PL (1.68×10^{-4} S

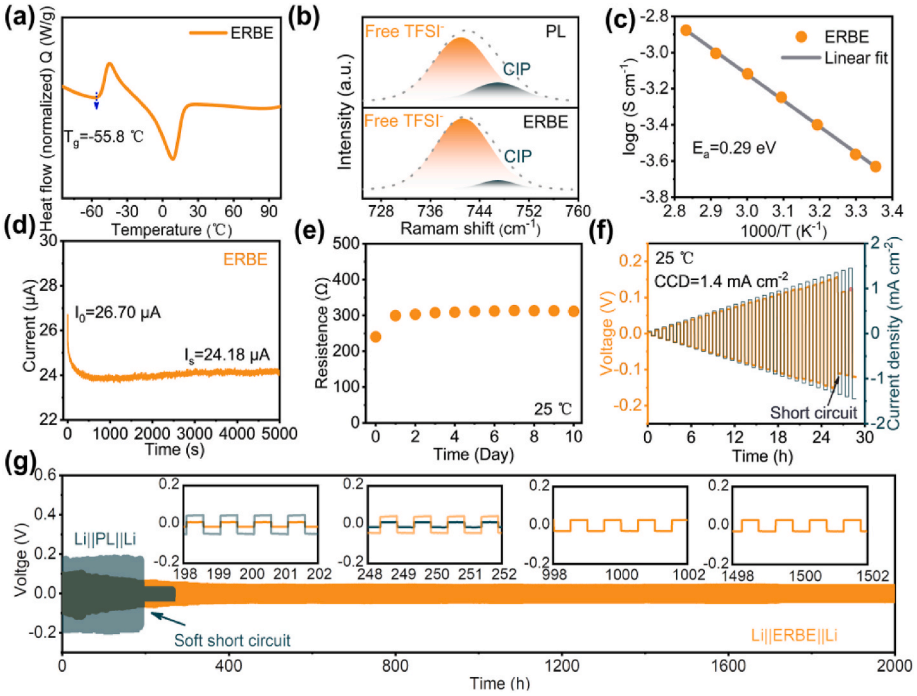

Fig. 3. (a) Differential scanning calorimetry (DSC) curve of ERBE from −80 °C to 100 °C and 10 °C min^{-1}. (b) Raman spectra of PL and ERBE. (c) Li-ions conductivities of ERBE at varying temperatures. (d) Chronoamperometry curve of Li||ERBE||Li symmetrical cells under polarization voltage of 10 mV and 25 °C. (e) Electrochemical impedance of ERBE-based Li deposition/stripping test at 0.5 mA cm^{-2} and 25 °C.

cm^{-1}), and the corresponding activation energies are lower for ERBE (0.29 eV) than that of 0.32 eV for PL. As shown in Fig. 3d and S10, the impedance of the Li||ERBE||Li before and after polarization is 276.8 and 254.8 Ω, respectively, the corresponding Li-Ions transfer number is as high as 0.69. The above results indicate that the additive of PEGDA has a positive effect on the Li-ions conduction of ERBE electrolyte. The changes in static interfacial impedance between ERBE electrolyte and lithium metal anode with time was observed and showed in Fig. S11. The initial impedance value of Li||ERBE||Li cells is only 246.73 Ω, due to the transformation of the ERBE precursor from liquid to solid during heat treatment, the impedance value increases slightly to 299.52 Ω, and remains stable in the subsequent 9 days of resting (Fig. 3e). The low and stable interfacial impedance suggests that ERBE electrolyte has good affinity and chemical stability with lithium metal anode. Critical current density (CCD) also works as an important index to assess the performances of Li metal anodes at high current densities in solid-state batteries. As shown in Fig. 3f, the CCD of Li||ERBE||Li cell reaches as high as 1.4 mA cm^{-2}, which is over 2 times higher than that of Li||PL||Li cells (Fig. S12). Fig. 3g shows the long-term deposition/stripping of Li-symmetric cells. The cells cycled with PL electrolyte exhibit high voltage polarization of up to 195 mV during the first 200 h cycling, subsequently suffered short-circuit and the battery failed. In contrast, the cells life with ERBE electrolyte was greatly increased to 2000 h and maintained a low overpotential of 30 mV all the time. The above results exceed most polymer electrolytes reported in the literature (Table S2).

3.3. Characterization of the compatibility with high-loading cathode

The suitability between solid-state electrolyte and high-loading cathode is a prerequisite to achieving the high energy density SSLBs. The performance of high-loading cathode as prepared by the traditional slurry coating process was first evaluated before and after rolling pressing. As depicted in Fig. 4a and b, the LFP cathode electrode (78 mg cm^{-2}) without rolling pressing exhibits a loosely porous structure, after rolling pressing, the porosity was significantly reduced and the structure became dense the shows. As seen in Fig. 4c and S13, the contact angle of the ERBE precursor fluid with the LFP cathode changed slightly before and after rolling, increasing only from 4.8° to 5.2°, indicating that the densification treatment of thick LFP cathodes hardly affects the wettability with ERBE precursor. To visualize the distribution of ERBE within the thick electrodes, S elements from LiTFSI were examined as a characteristic element by EDS mapping and cross-sectional SEM. As seen in Fig. 4d, S element is uniformly distributed in ERBE and LFP thick electrodes, while Fe element only exists in thick electrodes, which further proves the strong penetration ability of ERBE. As expected, the rolling pressing treatment promotes the continuity of the particles within the thick electrodes, and the impedance is significantly reduced to 942 Ω, which is much lower than the 1765 Ω before rolling pressing (Fig. 4e). However, the impedance of the LFP||ERBE||LFP cells constructed with the ex-situ method is over 9218 Ω (Fig. S14). To further examine the compatibility of the ERBE electrolyte with the high-loading cathode, the electrochemical performance of the cells with different mass loadings were tested. To investigate the compatibility of ERBE with high-loading cathodes, LFP||ERBE||Li cells with cathode mass loading of 11, 20, 40, 61, and 78 mg cm^{-2} were employed to charge and discharge at 0.1 C, and the corresponding current densities were 0.187, 0.342, 0.679, 1.036, and 1.326 mA cm^{-2}. As shown in Fig. 4f, the discharge capacities are as high as 1.89, 3.43, 6.77, 10.95, and 11.98 mAh cm^{-2},

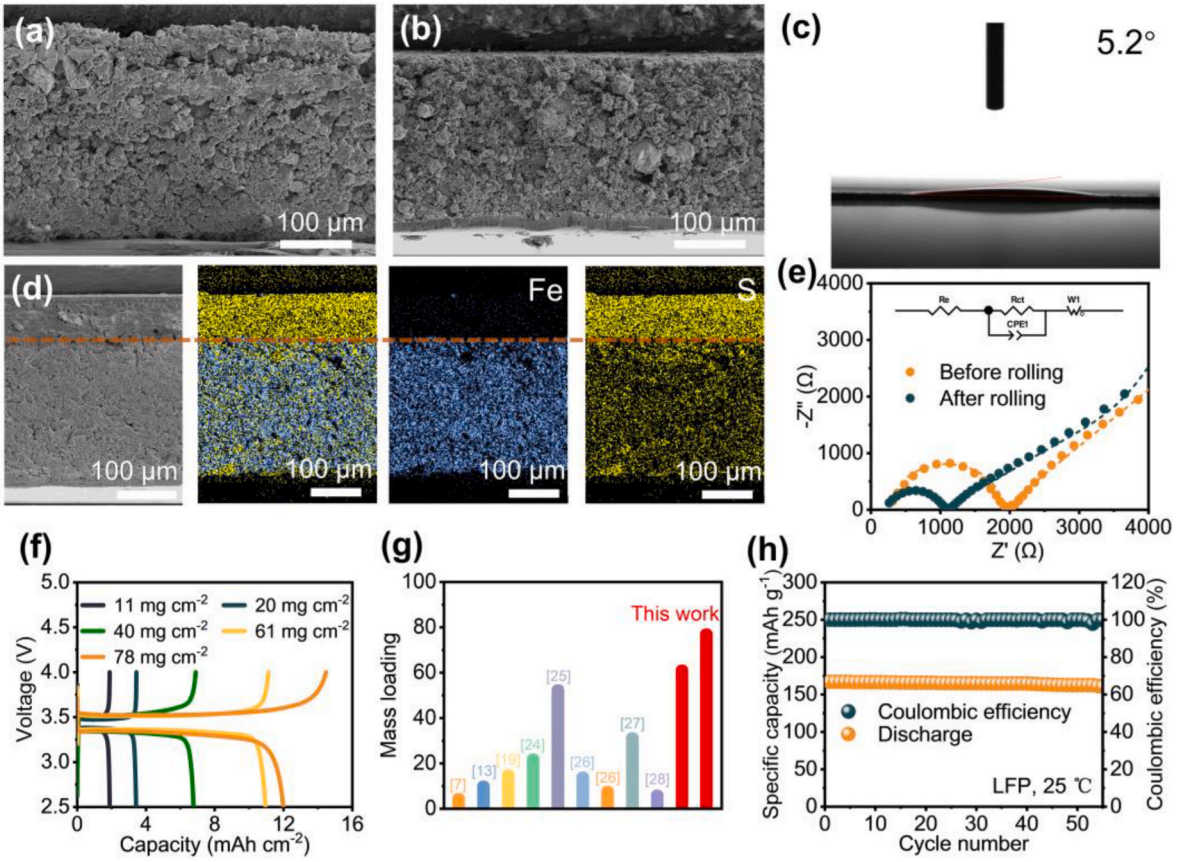

Fig. 4. LFP cathodes electrodes at 78 mg cm^{-2} mass loading. (a–b) Before and after rolling pressing. (c) Contact angle test of ERBE precursor with high-loading LFP electrode after rolling pressing. (d) SEM and EDS images of LFP/ERBE interface. (e) Nyquist impedance plots of LFP||ERBE||LFP cells at 25 °C. (f) Charge-discharge curves with different mass loadings of LFP electrode. (g) Comparison of ERBE matched mass loadings with those of cells previously reported. (h) Cycling performance of LFP||ERBE||Li cells with 16.43 mg cm^{-2} at 25 °C.

respectively, which are much higher than the results reported in the literature for high-loading SSLBs (Fig. 4g). At the mass loading of 16.43 mg cm^{-2}, the cycling stability test of LFP||ERBE||Li cell was performed at 0.1 C (0.279 mA cm^{-2}). As shown in Fig. 4h, the LFP||ERBE||Li cells contribute a high initial discharge capacity of 166.9 mAh g^{-1}, which is close to the theoretical specific capacity of LFP (1 C = 170 mAh g^{-1}), and after 55 cycles, the capacity retention rate is as high as 96.4 % and the polarization voltage is low to 85 mV (Fig. S15). It is shown that the ERBE precursor penetrates well with the high-loading cathode and maintained excellent contact and stability after in-situ heat curing [24–29].

3.4. Stability of electrode/electrolyte interfaces

To further analyze the key role of the electrode-electrolyte interfaces for the stable cycling of the batteries, the morphologies of ERBE and cathode/lithium metal anode interfaces were observed from the disassembled cells after 200 cycles at 1 C. As seen in Fig. 5a, the SEM image indicated that the surface of the cathode was uniformly covered by ERBE electrolyte after cycling. The cross-sectional SEM image in Fig. 5b further reveals the good permeability of the ERBE precursor with LFP electrode, and the stability of ERBE during cycling process. The suitable combination of electrolyte and cathode materials can provide the Li-ions transport channels to compensate the discontinuous transport in thick electrodes (Fig. 5c). Likewise, the cycled lithium metal anode surface is also covered with uniform ERBE, showing a smooth morphology without visible dendrites deposit after cycling and formed tight interfacial contacts (Fig. 5d–f). In contrast, the surface of lithium metal anode with PL electrolyte cycled became rough and exhibited significant by-products caused by inhomogeneous Li-ions deposition/stripping during cycling (Fig. S16). In addition, due to the uneven deposition/stripping of lithium metal anode during cycling, the surface of PL electrolyte membrane shows massive irregular and lumpy morphology (Fig. S17a), while the ERBE diaphragm features a smoothly flattened surface without deposit residue (Fig. S17b). The results show that the ERBE electrolyte is favorable for guiding the Li-ions homogeneous transport and deposition. Fig. 5g–i shows the XPS spectra of F, S, and C elements for the cycled lithium metal anode surface. After peak-fitting analysis, a large number of organic components were detected, including $–CF_3$ (292.48 eV, C 1s), C–C (284.60 eV, C 1s), C–O (285.72 eV, C 1s), and C═O (287.21 eV, C 1s) in the Li surface cycled with ERBE. In addition, significant amounts of inorganic components, including Li_2CO_3 (290.70 eV, C 1s), LiF (684.80 eV, F 1s) were also observed in the corresponding spectra of cycled lithium metal anode. More importantly, two peaks of Li_2S and Li_2S_x produced by the decomposition of the $TFSI^-$ appeared on the lithium metal anode surface after cycled with PL (Fig. S18). However, these peaks were not found on the lithium metal anode surface cycled with ERBE. The lithium metal surfaces disassembled from the cycled Li||ERBE||Li cells were further analyzed by TEM images and EDS mapping. As shown in Fig. S19, the inorganic components including Li_2CO_3, LiF, and Li_2SO_3 were identified in the TEM image and corresponding to the (200), (200), and (114) crystal faces, respectively. The uniform distribution of N, F, S elements in the detection region was also observed in EDS mapping. The results show that the introduction of an appropriate number of PS into the electrolyte can protect LiTFSI from decomposition

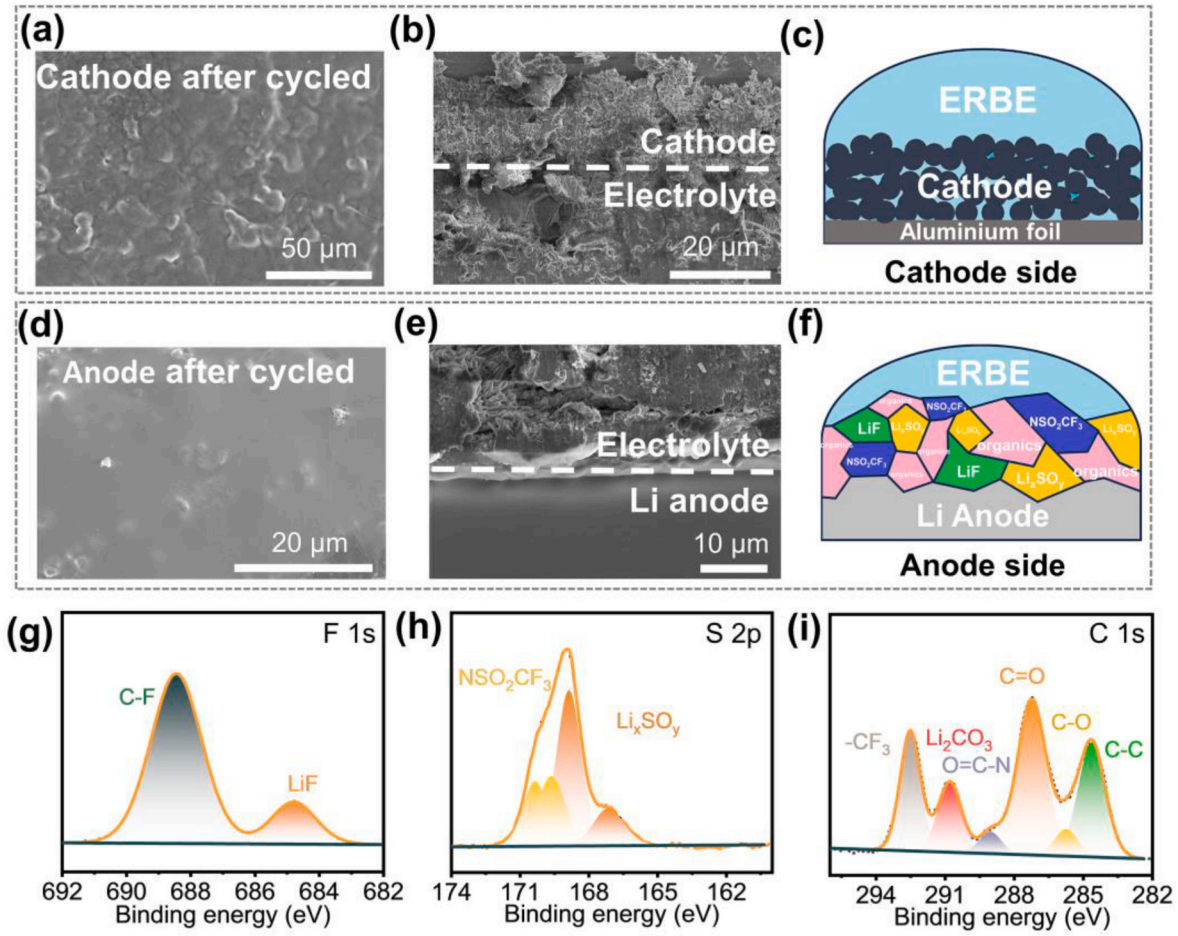

Fig. 5. (a–c) SEM images of LFP surface and LFP/ERBE interface, and schematic of the corresponding cathode interfacial layer after cycling. (d–f) SEM images of lithium metal anode surface and Li/ERBE interface, and schematic of the corresponding lithium metal anode interfacial layer. (g–i) XPS analysis of F, S, C elements for lithium metal anode disassembled from LFP||ERBE||Li cells after 200 cycles at 1 C.

during cycling, which provides coordination support for the stable transport of Li-ions.

3.5. Cycle and rate performances of LFP||ERBE||Li cells

To further understand the electrochemical performance of ERBE in SSLBs, rate and cycle performances were performed on coin and pouch cells. Fig. 6a displays the voltage curve of the LFP||ERBE||Li in the range of −20 °C–60 °C at 0.1 C. The discharge capacity at 25 °C and 60 °C were 163.8 and 168.8 mAh g^{-1} respectively, even at −20 °C, it still can provide a high discharge specific capacity of 86.7 mAh g^{-1}. As seen in Fig. 6b and S20, the discharge specific capacity of LFP||ERBE||Li cells at 0.1, 0.2, 0.5, 1 and 2 C were 165.6, 162.3, 152.4, 140.8 and 132.2 mAh g^{-1}, respectively, when the current density returned to 0.2 C, the capacity was recovered to 160.6 mAh g^{-1}. The results of a long cycle test at −10 °C showed that LFP||ERBE||Li cells can provide a high capacity retention of 97.3 % after 230 cycles at 0.1 C (Fig. 6c). At 25 °C, the LFP||ERBE||Li cells show a high discharge specific capacity of 126.0 mAh g^{-1} after 500 cycles at 0.2 C (Fig. S21). Fig. 6d displays the long-term cycling performance at 1 C, LFP||ERBE||Li cells delivered an initial discharge capacity of up to 140.7 mAh g^{-1} with a high average coulomb efficiency (99.9 %), after 1400 and 3000 cycles, the capacity retention was 80 % and 70.1 %, respectively, and even after 4000 cycles, it still can deliver a discharge capacity of 75.6 mAh g^{-1}. As a comparison, the LFP||PL||Li cells have an average coulombic efficiency of only 86.1 % over 200 cycles (Fig. S22). At 60 °C, the LFP||ERBE||Li cells can be stably cycled over 300 times with a high initial discharge capacity of 134.8 mAh g^{-1} and 93.8 % capacity retention at 2 C (Fig. S23). The above results are significantly superior to the recently reported in-situ polymer electrolytes (Table S3). Considering that ERBE shows wide electrochemical window of 4.58 V (Fig. S24), the high-voltage NCM333||ERBE||Li cells were assembled, as shown in Fig. S25, the cells exhibit high discharge capacities of 162.1 mAh g^{-1} at 25 °C and 122.4 mAh g^{-1} at −10 °C. The corresponding excellent rate and cycle performances can be found in Figs. S26 and S27. To further investigate the potential utility of ERBE, a 4 × 4 cm^2 LFP||ERBE||Li pouch cells with different mass loadings were further fabricated. As seen in Fig. 6e, at the mass loadings of 4,10,15 and 20 mg cm^{-2}, the pouch cells offered 7.9, 25.9, 38.3 and 50.1 mAh respectively. A cycling performance test at the mass loading of 7.64 mg cm^{-2}, showing that the pouch cells have a high discharge capacity of 20.35 mAh and a coulombic efficiency of up to 99.7 % after 20 cycles (Fig. 6f). After treatment with extreme tests of folding, drilling and shearing, the battery was still able to make the LED continued to emit a stable light, highlighting the reliability and stability of the battery in extreme environments (Fig. 6g).

4. Conclusions

In summary, an elasticity-rigidity balanced polymer electrolyte (ERBE) was designed by in-situ polymerized VC monomer and PEGDA crosslinker. The introduction of PEGDA greatly improves the intrinsic elasticity of the PVC-based electrolyte, the critical compression ratio is up to 73.9 %, corresponding to a high compressive strength of 96.1 MPa. The ERBE precursor has excellent wettability with thick cathode and

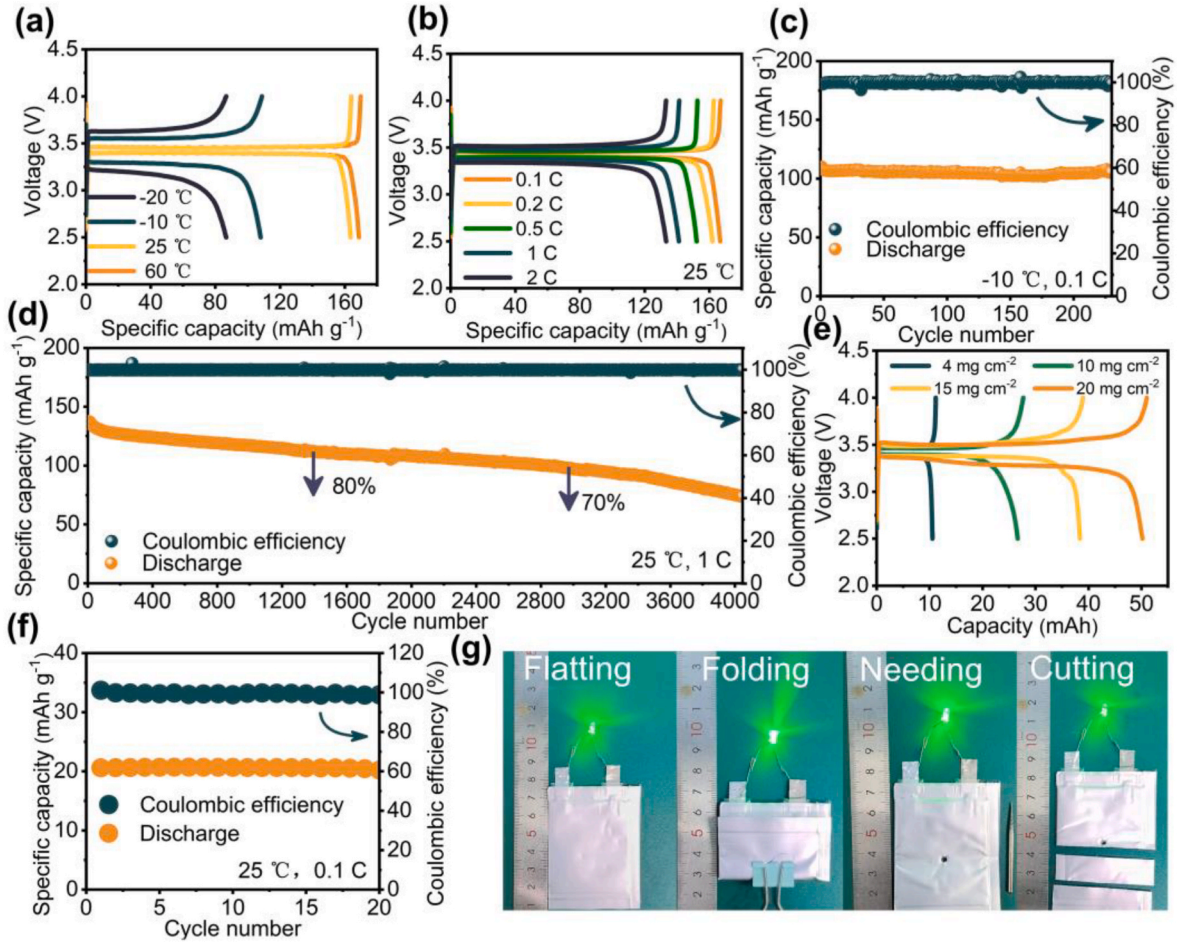

Fig. 6. LFP||ERBE||Li cells of (a) Charge-discharge curves with different temperatures. (b) Rate performance at 25 °C. (c) Cycle performance at −10 °C. (d) Cycle performance at 25 °C. (e) Charge-discharge curves of LFP||ERBE||Li pouch cells at 25 °C. (f) Cycle performances of LFP||ERBE||Li pouch cells at 25 °C. (g) Abusive testing of flexible pouch cells.

superior compatibility with lithium metal anode. The room temperature ionic conductivity and Li-ions transfer number of the ERBE are as high as 2.31×10^{-4} S cm^{-1} and 0.69, respectively. As expected, the ERBE was successfully matched to an ultra-high loading cathode of 78 mg cm^{-2} and provided a high capacity of 11 mAh cm^{-2}. The Li-symmetric cells were cycled stably for over 2000 h at 0.5 mA cm^{-2}. In the long-cycle performance test, LFP||ERBE||Li cells cycle over 4000 times with a coulombic efficiency over 99 % at 1 C and 25 °C. The elasticity-rigidity in-situ polymer electrolyte with excellent flexibility and the rigidity required to inhibit dendrite growth, which is a practical reference for the design of long-cycle, wide-temperature, high-energy-density solid-state lithium-metal batteries.

CRediT authorship contribution statement

Weichen Han: Writing – original draft, Data curation. **Jingang Zheng:** Writing – original draft, Data curation. **Hao Huang:** Methodology, Formal analysis. **Hongxu Zhou:** Validation, Investigation. **Hongyang Li:** Investigation. **Han Zhang:** Visualization, Conceptualization. **Lixiang Li:** Supervision. **Weimin Zhou:** Visualization, Validation. **Baigang An:** Validation, Supervision, Funding acquisition. **Chengguo Sun:** Writing – review & editing, Validation, Supervision, Funding acquisition.

Declaration of competing interest

The authors declare no conflict of interest.

Data availability

Data will be made available on request.

Acknowledgments

The authors gratefully acknowledge financial supported by the National Natural Science Foundation of China (11972178, 52371224).

Appendix A. Supplementary data

Supplementary data to this article can be found online at https://doi.org/10.1016/j.memsci.2024.123374.

References

[1] Z.Y. Wang, J.L. Xia, X. Ji, Y.J. Liu, J.X. Zhang, X.Z. He, W.R. Zhang, H.L. Wan, C. S. Wang, Lithium anode interlayer design for all-solid-state lithium-metal batteries, Nat. Energy 9 (2024) 251–262.
[2] A.G. Nguyen, C.J. Park, Insights into tailoring composite solid polymer electrolytes for solid-state lithium batteries, J. Membr. Sci. 675 (2023) 30.
[3] L.F. Tang, B. Chen, Z.H. Zhang, C. Ma, J.C. Chen, Y. Huang, F. Zhang, Q.Y. Dong, G. Y. Xue, D. Chen, C. Hu, S. Li, Z. Liu, Y.B. Shen, Q. Chen, L. Chen, Polyfluorinated crosslinker-based solid polymer electrolytes for long-cycling 4.5V lithium metal batteries, Nat. Commun. 14 (2023) 10.
[4] W.L. Xu, R.B. Dang, L. Zhou, Y. Yang, T. Lin, Q.B. Guo, F. Xie, Z.L. Hu, F.X. Ding, Y. P. Liu, Y. Liu, H.C. Mao, J. Hong, Z.C. Zuo, X.Q. Wang, R. Yang, X. Jin, X.Y. Hou, Y. X. Lu, X.H. Rong, N. Xu, Y.S. Hu, Conversion of surface residual alkali to solid electrolyte to enable Na-Ion full cells with robust interfaces, Adv. Mater. 35 (2023) 9.
[5] J.K. Hu, Y.C. Gao, S.J. Yang, X.L. Wang, X. Chen, Y.L. Liao, S. Li, J. Liu, H. Yuan, J. Q. Huang, High energy density solid-state lithium metal batteries enabled by in situ polymerized integrated ultrathin solid electrolyte/cathode, Adv. Funct. Mater. 11 (2024).
[6] K. Liang, H.S. Zhao, J.B. Li, X.B. Huang, S.Y. Jia, W.K. Chen, Y.R. Ren, Engineering crystal growth and surface modification of $Na_3V_2(PO_4)_2F_3$ cathode for high-energy-density sodium-ion batteries, Small 19 (2023) 9.
[7] G.J. Lu, W. Liu, Z.G. Yang, Y.M. Wang, W.K. Zheng, R.R. Deng, R.H. Wang, L. Lu, C. H. Xu, Superlithiophilic, ultrastable, and Li-ions-conductive interface enabled long lifespan all-solid-state lithium-metal batteries under high mass loading, Adv. Funct. Mater. 33 (2023) 13.
[8] X.Y. Tang, X.S. Xu, M. Bai, M. Zhang, H.L. Wang, Z.Q. Wang, A.H. Shao, H. Q. Wang, Y. Ma, Ultrafast laser-induced cathode/electrolyte interphase for high-voltage poly(ethylene oxide)-based solid batteries, Adv. Funct. Mater. 33 (2023) 11.
[9] W.K. Li, D.Y. Cheng, R. Shimizu, Y.X. Li, W.L. Yao, G. Raghavendran, M.H. Zhang, Y.S. Meng, Artificial cathode electrolyte interphase for improving high voltage cycling stability of thick electrode with Co-free 5 V spinel oxides, Energy Storage Mater. 49 (2022) 77–84.
[10] Y.J. Sun, W.J. Huang, G.F. Zhao, Q. Liu, L.Y. Duan, S.M. Wang, Q. An, H. Wang, Y. X. Yang, C.H. Zhang, H. Guo, $LiNi_{0.9}Co_{0.09}Mo_{0.01}O_2$ cathode with Li_3PO_4 coating and Ti doping for next-generation lithium-ion batteries, ACS Energy Lett. 8 (2023) 1629–1638.
[11] Y.K. Wei, B. Tang, X. Liang, F. Zhang, Y.B. Tang, An ultrahigh-mass-loading integrated free-standing functional all-carbon positive electrode prepared using an architecture tailoring strategy for high-energy-density dual-ion batteries, Adv. Mater. 35 (2023) 11.
[12] Y. Liu, X.F. An, K. Yang, J.B. Ma, J.S. Mi, D.F. Zhang, X. Cheng, Y.H. Li, Y.T. Ma, M. Liu, F.Y. Kang, Y.B. He, Achieving a high-loading of cathode in PVDF-based solid-state battery, Energy Environ. Sci. 17 (2024) 344–353.
[13] G.Z. Cheng, H. Sun, H.R. Wang, Z.Y. Ju, Y. Zhu, W.Q. Tian, J.W. Chen, H.L. Wang, J.Y. Wu, G.H. Yu, Efficient ion percolating network for high-performance all-solid-state cathodes, Adv. Mater. (2024) 10.
[14] K.S. Oh, S. Park, J.S. Kim, Y. Yao, J.H. Kim, J. Guo, D.H. Seo, S.Y. Lee, Electrostatic covalent organic frameworks as on-demand molecular traps for high-energy Li metal battery electrodes, ACS Energy Lett. 8 (2023) 2463–2474.
[15] J.H. Kim, K.M. Lee, J.W. Kim, S.H. Kweon, H.S. Moon, T. Yim, S.K. Kwak, S.Y. Lee, Regulating electrostatic phenomena by cationic polymer binder for scalable high-areal-capacity Li battery electrodes, Nat. Commun. 14 (2023) 13.
[16] X.A. Zhou, F.L. Zhang, X.L. Fu, N.S. Zhang, J. Huang, X.P. Cai, H. Ding, B.Q. Li, L. Niu, S.Y. Li, Utilizing fast ion conductor for single-crystal Ni-rich cathodes to achieve dual-functional modification of conductor network constructing and near-surface doping, Energy Storage Mater. 52 (2022) 19–28.
[17] X.F. An, Y. Liu, K. Yang, J.S. Mi, J.B. Ma, D.F. Zhang, L.K. Chen, X.T. Liu, S.K. Guo, Y.H. Li, Y.T. Ma, M. Liu, Y.B. He, F.Y. Kang, Dielectric filler-induced hybrid interphase enabling robust solid-state Li metal batteries at high areal capacity, Adv. Mater. 36 (2024) 12.
[18] K.J. Wang, Z.T. Liang, S.T. Weng, Y. Ding, Y. Su, Y.Q. Wu, H.Y. Zhong, A. Fu, Y. Sun, M.Z. Luo, J.W. Yan, X.F. Wang, Y. Yang, Surface engineering strategy enables 4.5 V sulfide-based all-solid-state batteries with high cathode loading and long cycle life, ACS Energy Lett. 8 (2023) 3450–3459.
[19] J.H. Kim, J.M. Kim, S.K. Cho, N.Y. Kim, S.Y. Lee, Redox-homogeneous, gel electrolyte-embedded high-mass-loading cathodes for high-energy lithium metal batteries, Nat. Commun. 13 (2022) 11.
[20] Z. Li, J.L. Fu, X.Y. Zhou, S.W. Gui, L. Wei, H. Yang, H. Li, X. Guo, Li-ions conduction in polymer-based solid electrolytes, Adv. Sci. 10 (2023) 18.
[21] J. Bae, X. Zhang, X.L. Guo, G.H. Yu, A general strategy of anion-rich high-concentration polymeric interlayer for high-voltage, all-solid-state batteries, Nano Lett. 21 (2021) 1184–1191.
[22] X.X. Xie, Z.X. Wang, S. He, K.J. Chen, Q. Huang, P. Zhang, S.M. Hao, J.T. Wang, W. D. Zhou, Influencing factors on Li-ions conductivity and interfacial stability of solid polymer electrolytes, exampled by polycarbonates, polyoxalates and polymalonates, Angew. Chem.-Int. Edit. 62 (2023) 12.
[23] X. Zhang, M. Zhang, J. Wu, X. Hu, B. Fu, Z. Zhang, B. Luo, K. Khan, Z. Fang, Z. Xu, M. Wu, Lewis acid fluorine-donating additive enables an excellent semi-solid-state electrolyte for ultra-stable lithium metal batteries, Nano Energy 115 (2023).
[24] Q. Kang, Z.C. Zhuang, Y. Li, Y.Z. Zuo, J. Wang, Y.J. Liu, C.Q. Shi, J. Chen, H.F. Li, P.K. Jiang, X.Y. Huang, Manipulating dielectric property of polymer coatings toward high-retention-rate lithium metal full batteries under harsh critical conditions, Nano Res. 16 (2023) 9240–9249.
[25] L.D. Zhou, T.T. Zuo, C.Y. Kwok, S.Y. Kim, A. Assoud, Q. Zhang, J. Janek, L. F. Nazar, High areal capacity, long cycle life 4 V ceramic all-solid-state Li-ions batteries enabled by chloride solid electrolytes, Nat. Energy 7 (2022) 83–93.
[26] G.D. Zhou, J. Yu, F. Ciucci, In situ prepared all-fluorinated polymer electrolyte for energy-dense high-voltage lithium-metal batteries, Energy Storage Mater. 55 (2023) 642–651.
[27] Q. Liang, L.N. Chen, J.Y. Tang, X.Z. Liu, J.J. Liu, M. Tang, Z.B. Wang, Large-scale preparation of ultrathin composite polymer electrolytes with excellent mechanical properties and high thermal stability for solid-state lithium-metal batteries, Energy Storage Mater. 55 (2023) 847–856.
[28] Y. Ishiguro, K. Ueno, S. Nishimura, G. Iida, Y. Igarashib, $TaCl_5$-glassified ultrafast lithium ion-conductive halide electrolytes for high-performance all-solid-state lithium batteries, Chem. Lett. 52 (2023) 237–241.
[29] W.D. Bao, Y. Zhang, L. Cao, Y.L. Jiang, H. Zhang, N. Zhang, Y. Liu, P. Yan, X. Z. Wang, Y.X. Liu, H.Y. Li, Y.B. Zhao, J. Xie, An H_2O-initiated crosslinking strategy for ultrafine-nanoclusters-reinforced high-toughness polymer-in-plasticizer solid electrolyte, Adv. Mater. 35 (2023) 9.